Journal of Electroceramics 3:4, 433–441, 1999

Characterization and Electrochemical Studies of $LiMn_2O_4$ Cathode Materials Prepared by Combustion Method

S. CHITRA, P. KALYANI, T. MOHAN & R. GANGADHARAN
Central Electrochemical Research Institute, 630006 Karaikudi, India

B. YEBKA, S. CASTRO-GARCIA, M. MASSOT & C. JULIEN
Laboratoire des Milieux Désordonnés et Hétérogènes, UMR-CNRS 7603, Université Pierre et Marie Curie, 4 place Jussieu, 75252 Paris cedex 05, France

M. EDDRIEF
Laboratoire de Minéralogie et Cristallographie, Université Pierre et Marie Curie, 4 place Jussieu, 75252 Paris cedex 05, France

Submitted August 12, 1998; Revised June 10, 1999; Accepted July 4, 1999

Abstract. A combustion method using urea as a fuel has been developed for the synthesis of the spinel $LiMn_2O_4$ around 500°C. Physical features of the products were identified by X-ray photoelectron spectroscopy, X-ray diffractometry, Raman scattering and FTIR spectroscopy. Cells were fabricated with $Li//LiMn_2O_4$ and $C//LiMn_2O_4$ in nonaqueous organic electrolyte and their performances were studied. A kinetic profile for diffusion of Li ions in the composite matrix was developed and tested.

Keywords: $LiMn_2O_4$ spinel, Raman, FTIR, XPS, lithium-ion batteries

1. Introduction

Lithium manganese oxide $LiMn_2O_4$ with the $A[B_2]O_4$ spinel structure is a well-known cathode material used in high energy density batteries for high power and medium-sized cell applications [1–7]. This compound is presently among the most widely studied materials for secondary batteries. It has an atacamite-type structure [8] and often referred to as spinel [9]. $LiMn_2O_4$ is exploited very much as a battery cathode in lithium-ion cells due to its availability, non toxicity, least environmental hazards besides cheapness compared to its counterpart materials like $LiCoO_2$ and $LiNiO_2$. The spinel phase belongs to the Li-Mn-O system, which has been studied in detail as insertion electrode for secondary lithium cells. This system exists in various phases having a general formula $Li_{1+\partial-x}Mn_{2-\partial}O_4$, in which lithium ions occupy the 8a tetrahedral interstices and the manganese cations occupy the 16d octahedral interstices of a cubic close-packed array constituted by the oxygen atoms located in the 32e positions of the Fd3m space group [10,11]. In addition, there are vacant 16c octahedral and 48f and 8b tetrahedral interstices. The classical intercalation/deintercalation reactions in the electrochemical $Li//LiMn_2O_4$ cell can be written as

$$\square[Mn^{+4}]_2O_4 + Li \leftrightarrow Li[Mn^{+3.5}]_2O_4 \quad (1)$$

$$Li[Mn^{+3.5}]_2O_4 + Li \leftrightarrow Li_2[Mn^{+3}]_2O_4 \quad (2)$$

which normally lie in between the voltage 4.0 and 3.0 V, respectively [5]. In Eqs. (1) and (2) the brackets denote species in octahedral B sites, as is usual in spinel structure chemistry.

$LiMn_2O_4$ spinel can be synthesized by many methods [10–16]. $LiMn_2O_4$ is prepared by the solid-state reactions between compounds of lithium and manganese, i.e., nitrates, oxides and carbonates at a temperature range of 800–1000°C. In these methods all the solid particles may not altogether react

resulting in undesirable impurities in the final product. Since the particle size and surface area of the resulting product cannot be controlled using a high temperature synthesis, low temperature procedures were suggested recently [16]. These techniques were using either citrate, tartrate, maliate, or malanate of lithium and manganese salts.

In this paper, we report the synthesis and characterization of $LiMn_2O_4$ obtained in a pure state by a solution technique using inorganic salts [17,18]. The composition and the structural properties have been characterized by X-ray diffractometry (XRD), X-ray photoelectron spectroscopy (XPS), scanning electron microscopy (SEM), and vibrational spectroscopies, i.e., Raman scattering (RS) and Fourier transform infrared (FTIR). The latter techniques provide information on the local environment of the atoms in the lattice. The suitability of $LiMn_2O_4$ as cathode have been tested by fabricating a lithium cell using nonaqueous electrolyte and the electrochemical parameters have been studied. The performance of a lithium-ion cell is also reported.

2. Experimental

2.1. *Preparation of the* $LiMn_2O_4$ *Spinel*

The nitrates of Li and Mn were taken in equimolar proportions, mixed together and dissolved in a low boiling organic solvent. The organic solvent in this solution was evaporated off and the resulting mass was initially heated to 100°C and finally heated at 300°C to decompose the product to obtain the end product $LiMn_2O_4$, which is of high purity [11]. This compound may contain still some impurity due to the influence of reduction of oxides by organic media. In order to avoid this contamination a purely inorganic route was formulated. Stoichiometric amounts of Li and Mn nitrates with urea were mixed and dissolved in aqueous solution. Then, this solution was evaporated to dryness and calcined for few hours to decompose the mixture to get pure $LiMn_2O_4$ product. The product obtained was fine grained material of micrometer size and the yield was above 96% [17,18].

2.2. *Instruments*

XPS measurements were made using an ISA-Riber Mac 2 electron spectrometer with Mg K_α radiation (1253.6 eV). The binding energy was calibrated with reference to the C 1 s level of carbon (285.0 eV). XRD patterns were obtained with a Philips PW1830 X-ray diffractometer using nickel-filtered Cu K_α radiation. The diffraction patterns were taken at room temperature in the scan range of $10° < 2\theta < 80°$ using step scans. The step size and the scan rate were set at 0.1 and 0.2 degree/min, respectively.

Room-temperature RS spectrum was collected in a quasi-backscattering configuration on the powder sample annealed at 500°C. A Jobin-Yvon model U1000 double monochromator with holographic gratings and a computer-controlled photon-counting system was used. The laser light source was the 514.5 nm line radiation from a Spectra-Physics 2020 argon-ion laser. A RS spectrum is the average of 12 scans obtained with a spectral resolution of $2\,cm^{-1}$. The RS spectrum was recorded with a low power laser excitation of 15 mW to prevent any decomposition of the sample. FTIR absorption spectrum was recorded using a Brucker IFS113 v interferometer at a spectral resolution $2\,cm^{-1}$. In the far-infrared region, the spectrometer was equipped with a 3.5 μm-thick beam splitter, a globar source, and a DTGS/PE detector. Samples were ground to fine powders painted onto polyethylene slabs.

2.3. *Electrochemical Measurements*

Electrochemical studies were carried out on the synthesized product annealed at 500°C in order to test its suitability as cathode-active material in high voltage lithium-containing batteries as well as to measure quantitatively the energy content (capacity in mAh/g), the so-called electrochemical capacity of the synthesized spinel product. The test cells were fabricated in both $Li//LiMn_2O_4$ and $C//LiMn_2O_4$ configurations employing a non-aqueous Li^+ ion conducting organic electrolyte. Electrochemical cells were fabricated as follows. The typical composite cathode consisted of the mixture of spinel-$LiMn_2O_4$ powders (500°C), acetylene black and colloidal PTFE binder in the 90:5:5 weight ratio. The PTFE-acetylene black was used to provide good electrical conductivity as well as mechanical toughness between active grains. The above mixture was pressed onto an expanded aluminium microgrid at a pressure of $5\,tons\,cm^{-2}$. This procedure yields circular pellet electrodes of 13 mm diameter. The pellets were then dried at 120°C in air. Similarly, the carbonaceous

electrode was prepared using a natural graphite (from Prolabo). The active material was well mixed with the PTFE binder in the mass ratio 90:10 and pressed onto a copper mesh and subsequently dried at 120°C. Celgard 2400 membrane was used as the separator between the cathode and the anode. The electrolyte was prepared by dissolving 1M $LiPF_6$ in 1:1 (v/v) mixture of ethylene carbonate (EC) and dimethyl carbonate (DMC), respectively. Electrodes and separators were soaked in the electrolyte before being housed in a laboratory-scale Teflon cell hardware. In order to assess their electrochemical performance, potentiostatic cyclic voltammograms were recorded at a slow scan mode in the potential range between 3.0 and 4.2 V using a Mac-Pile system.

3. Results and Discussion

3.1. XPS Characterization

The chemical composition of $LiMn_2O_4$ spinel annealed at 500°C was obtained by XPS measurements. XPS measurements are suitable for quantitative analysis of Li-Mn-O compounds because a first-order process is involved in the photoelectron emission [19]. The quantitative analysis of the $LiMn_2O_4$ is made from the integrated intensities of the Mn 2p and Li 1 s lines, which are observed with the peaks attributed to oxygen in the XPS spectrum. Figure 1(a–c) displays the XPS spectra of Mn 2p, O 1 s and Li 1 s core levels, respectively, for a $LiMn_2O_4$ spinel sample prepared at 500°C. The line of Li 1 s core level has a low intensity with a binding energy located at 55.3 eV (Fig. 1(a)), which is close to that of Li metal (54.8 eV). The line shape of the core level O 1 s is Gaussian-like with a binding energy of 530.4 eV (Fig. 1(b)). An energy separation of 11.6 eV is observed between the Mn $2p_{3/2}$ and Mn $2p_{1/2}$ states (Fig. 1(c)). Thus, the Mn $2p_{3/2}$ peak in $LiMn_2O_4$ is observed between those of MnO_2 (642.6 eV) and Mn_2O_3 (641.6 eV). The intensity ratio between XPS peaks Mn $2p_{3/2}$ and Mn $2p_{1/2}$ shows that the $LiMn_2O_4$ product has been synthesized and most closely resemble stoichiometric spinel material.

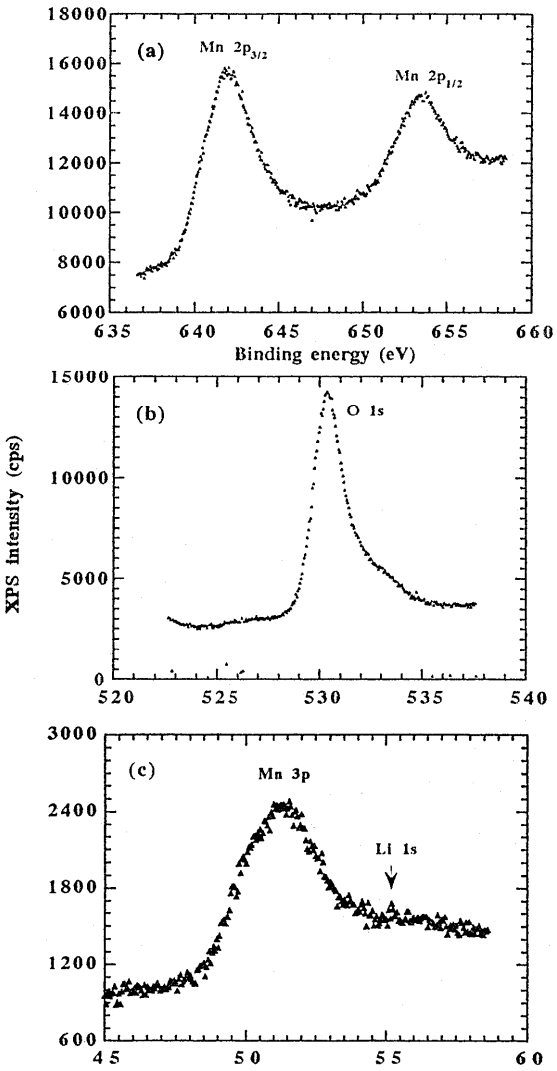

Fig. 1. X-ray photoelectron spectra of (a) Mn 2p, (b) O 1 s and (c) Li 1 s core levels for $LiMn_2O_4$ spinel prepared at 500°C.

3.2. XRD Characterization

Figure 2 shows the XRD diagram of $LiMn_2O_4$ spinel annealed at 500°C. This result confirms the formation of the spinel structure without any impurity phases (as far as XRD measurements are concerned) and the JCPDS data provide the exact search match based on Fd3m space group [4]. Considering the intensity and position of the peak attributed to the (400) line, we observed a good agreement between our results and those reported by other workers [7,20–22].

The XRD peaks of the spinel $LiMn_2O_4$ measured after annealing the product at 500°C were indexed assuming the cubic lattice constant $a = 8.24$Å. The degree of crystallinity was examined by measuring

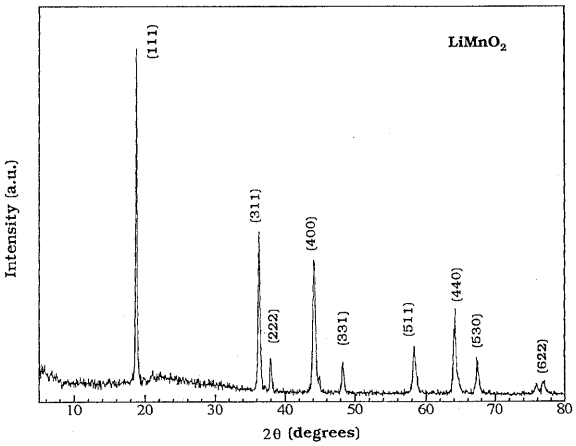

Fig. 2. X-ray diffraction patterns of microcrystalline $LiMn_2O_4$ powder.

the ex-situ diffractograms corresponding to the spinel product. Results indicate that the product obtained immediately after preparation gained the single-phase spinel structure without any residual impurities observable from XRD measurements. The peaks gradually sharpen with increasing annealing temperature, which indicates an increase of crystallinity as may occur from growth of grain size, ordering of local structure, and/or release of lattice strain.

To quantify the crystallite sizes (domain size) of the products, the full width at half maximum (FWHM) for (400) peak at ca. $2\theta = 44°$ was measured as this peak was found to be very sensitive to annealing temperature. The domain size became quite small (below 2 μm), indicating the low lattice strain when the sample is heat treated at 600°C. It is obvious that the lattice parameter initially varies smoothly as a result of structural ordering as the annealing temperature increases and remains constant for annealing between 500 and 600°C, where it attains a value of 8.24 Å. Further, as the annealing temperature rises, the lattice parameter increases sharply.

To measure the physical grain size of the spinel product, the SEM analysis was made out on sample annealed at 600°C. Figure 3 shows the scanning electron micrographs of the spinel $LiMn_2O_4$. The photograph (Fig. 3(b)) reveals the formation of spherical grains of micron-sized nature (average grain sizes being lower than 2 μm). A nearly pore-free state is evidenced from the micrograph. The grains are almost connected and ensured the high surface area. The aforementioned features are very desirable for an electrode material to be employed as a cathode-active material for the modern high energy Li-ion rechargeable batteries.

3.3. Spectroscopic Studies

The Raman scattering (RS) and Fourier transform infrared (FT-IR) spectra of the synthesized $LiMn_2O_4$ spinel recorded at room temperature are shown in Figs. 4(a) and 4b, respectively. The RS spectrum of $LiMn_2O_4$ (Fig. 4(a)) is dominated by a strong and broad band at ca. 625 cm^{-1} with a shoulder at 581 cm^{-1}. A band with a medium intensity appears at ca. 480 cm^{-1}, while four bands having a weak intensity are observed at ca. 364, 304, 198 and 154 cm^{-1}. The FTIR spectrum (Fig. 4(b)) is dominated by two strong absorption bands at ca. 622 and 513 cm^{-1}. Three weak bands are observed in the low frequency region at ca. 207, 277, and 370 cm^{-1}, and another weak band is observed at ca. 432 cm^{-1}.

The cubic spinel possesses Fd3m symmetry and has a general structural formula $Li[Mn_2]O_4$, where the manganese cations reside on the octahedral 16d sites, the oxygen anions on the 32e sites, and the lithium ions occupy the tetrahedral 8a sites. Analysis of the vibrational spectra of $LiMn_2O_4$ with Fd3m space group yields nine optic modes [23]. Five modes are Raman active $(A_{1g} + E_g + 3F_{2g})$ and four are infrared active (F_{1u}). It is also convenient to analyze these spectra in terms of localized vibrations, considering the spinel structure built of MnO_6 octahedra and LiO_4 tetrahedra [24]. Results are summarized in Table 1.

The Raman band located at ca. 625 cm^{-1} can be viewed as the symmetric Mn-O stretching vibration of MnO_6 groups. The position and the halfwidth of this band remain almost unchanged upon delithiation. This band is assigned to the A_{1g} symmetry in the O_h^7 spectroscopic space group. Its broadening may be related with the cation-anion bond lengths and polyhedral distortion occurring in $LiMn_2O_4$. The intensity of the shoulder located at 581 cm^{-1} increases upon lithium deintercalation. This may be due to the change of Mn^{3+} and Mn^{4+} proportion vs. x in the material. It is a fact that $Li[Mn^{3+}Mn^{4+}]O_4$ is a small-polaron semiconductor [25]. The RS peak at 304 cm^{-1} has the E_g symmetry, whereas the peaks located at 198, 364 and 480 cm^{-1} have the F_{2g} symmetry. The band at 154 cm^{-1} is attributed to the

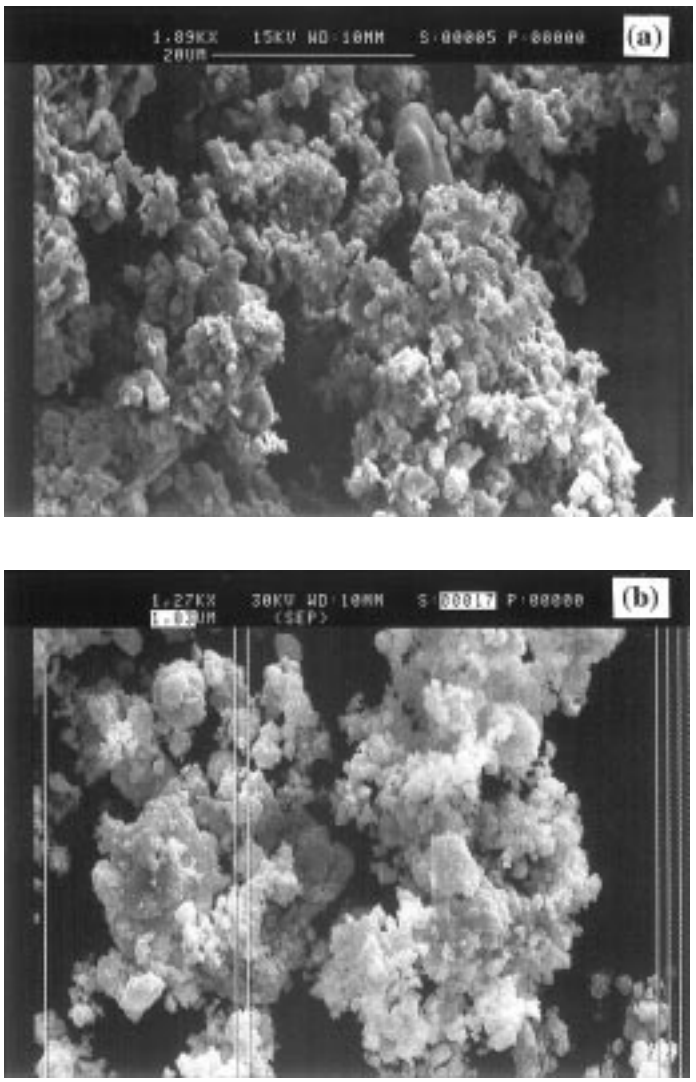

Fig. 3. Typical scanning electron micrographs of spinel $LiMn_2O_4$ annealed at temperature 600°C. The photograph (b) reveals the formation of spherical grains of micron-sized nature with an average grain sizes being lower than 2 μm.

lattice vibration involving bonding between MnO_6 units (internal mode).

The high-frequency bands of the FTIR absorption spectrum of $LiMn_2O_4$ located at ca. 622 and 513 cm^{-1} are attributed to the asymmetric stretching modes of MnO_6 group, whereas the low-frequency bands at ca. 207, 277 and 370 cm^{-1} are assigned to the bending modes of Mn-O. Because FTIR spectroscopy is capable of probing directly the near neighbor environment of the cation, we can study the local environment of lithium ions in this material [7,26,27]. It has been also demonstrated that the IR resonant frequencies of alkali metal cations in their equilibrium positions in inorganic oxide glasses are as cation mass dependent bands. Thus, the IR resonant frequency is related to the local force constant with an effective mass of vibration which is roughly that of alkali ion [28]. This leads to the frequency at ca. 432 cm^{-1} for the oscillation of the Li^+ ion with O^{2-} near neighbors in $LiMn_2O_4$.

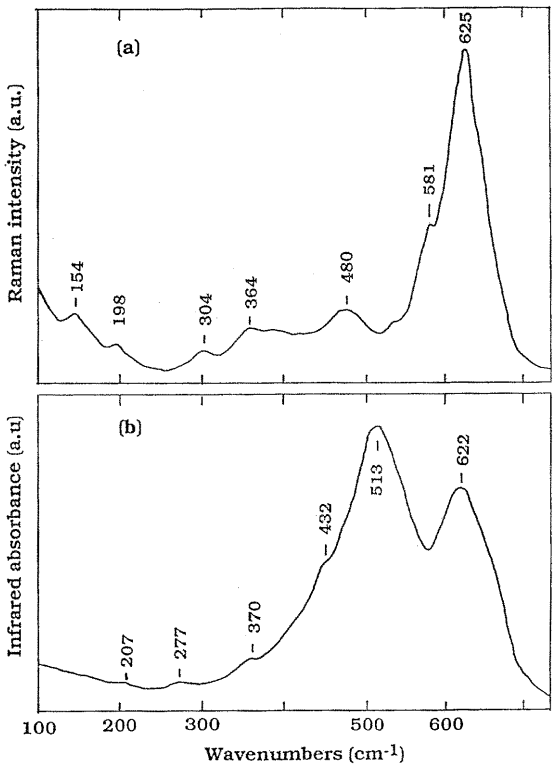

Fig. 4. Vibrational spectra of the spinel $LiMn_2O_4$. (a) Raman scattering spectrum recorded with the 514.5 nm line of an Ar-ion laser line at 15 mW power excitation. (b) FTIR absorption spectrum recorded at a spectral resolution 2 cm^{-1}.

It can be stated that in the ideal cubic spinel $LiMn_2O_4$, the Mn^{3+} and Mn^{4+} cations are considered as crystallographically equivalent (16d sites) in agreement with XRD data; then, occupation probabilities of 0.5 must be affected for each cation in 16d. Hence, a loss of translation invariance certainly occurs, due to local lattice distortions around the different Mn^{3+} and Mn^{4+} cations. As a result, a breakdown in the Raman and IR selection rules is expected, which may explain the observation of broad bands (disorder) and the fact that more modes than expected are observed in cubic $LiMn_2O_4$.

3.4. Electrochemical Charge-Discharge Features

The electrochemical behavior of synthesized spinel $LiMn_2O_4$ was examined in lithium-containing test cells employing a nonaqueous electrolyte medium. To begin with electrochemical measurements, the samples were first characterized by cyclic voltammetry on both Li//$LiMn_2O_4$ and C//$LiMn_2O_4$ cells. The voltammograms reveal the excellent reversibility of the cells containing spinel $LiMn_2O_4$. In the case of the Li//$LiMn_2O_4$ cell, the overall capacity improves upon repeated cycling which may presumably due to the formation of the stable passive protective layer onto lithium metal anode. As for the C//$LiMn_2O_4$ cell, the capacity fading is very nominal and the first irreversible loss is obviously due to graphite. This is a very common behavior when one deals with a carbon-based Li-ion rechargeable cells. As the cell is being cycled repeatedly, the irreversible loss becomes lesser.

In order to determine the electrochemical properties of the synthesized spinel used as cathode material, the Li//$LiMn_2O_4$ cells were subjected to constant current cycling 0.05 mA/cm^2. Figure 5 shows the first charge and discharge curves at 28°C of a Li//$LiMn_2O_4$ nonaqueous cell under galvanostatic conditions. In

Table 1. Wavenumbers (in cm^{-1}), intensities[a], and assignments of the Raman-active and IR-active modes of the spinel $LiMn_2O_4$

Raman	Intensity	IR	Intensity	Assignment
154	w			$\nu(MnO_6)$
198	w	207	w	δ_2(Mn-O)
		277	w	δ_1(Mn-O)
304	w			
364	w	370	w	
		432	w	ν_2(Li-O)
480	m			ν_1(Li-O)
		513	S	ν_4(Mn-O)
581	s			ν_3(Mn-O)
		622	S	ν_2(Mn-O)
625	S			ν_1(Mn-O)

[a]w = weak, m = medium, s = shoulder, S = strong.

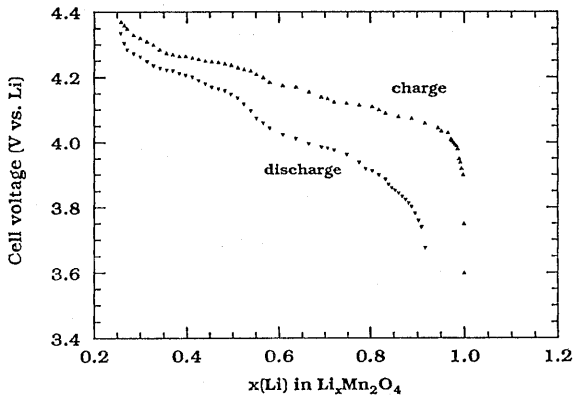

Fig. 5. Typical charge-discharge characteristics of Li//$LiMn_2O_4$ non-aqueous cell employing the electrolyte of composition 1M $LiPF_6$ in EC-DMC.(1:1) at room temperature. Charge and discharge were obtained at current density 0.05 mA/cm^2.

this voltage domain 3.0–4.5 V, the charge-discharge curves correspond to the voltage profiles characteristic of the spinel $LiMn_2O_4$ cathode material associated with lithium occupation of tetrahedral sites, in agreement with previous works [1,2,12]. The two characteristic regions indicating whether the delithiated $LiMn_2O_4$ exists as a single- or a multiple-phase are observed. The region (I) is characterized by an S-shaped voltage curve (at ca. 3.80–4.05 V), whereas the second region (II) corresponds to a plateau portion (at ca. 4.10 V) [24]. The upper 4-volt plateau provides over 110 mAh/g based on the active material utilization with an excellent cycleability.

After optimizing the active cathode material, i.e., the spinel $LiMn_2O_4$, the next step of the investigation involved a study of a laboratory-scale lithium-ion cell (rocking-chair cell). A lithium-ion cell includes two intercalation compounds as electrodes, with lithium ions shuttling back and forth between the positive and negative electrodes as the battery is charged and discharged. The C//$LiMn_2O_4$ Li-ion technology was shown to exhibit excellent room temperature cycle life (more than 1500 cycles), and good rate capabilities (the battery can deliver 95% of its total capacity at the 1 C discharge rate) [28]. A graphite-based Li-ion cell (C//$LiMn_2O_4$) was cycled in the galvanostatic mode at charging and discharging current densities of 0.3 and 0.15 mA/cm^2, respectively. After the assembly, such a cell was in the discharged state with an output voltage close to 0.5 V. The cell was activated during the first charge, when Li is de-intercalated from the spinel $LiMn_2O_4$ and intercalated to the carbon anode. The weight ratio of the positive and negative materials $w_{spinel}/w_{carbon} = 3$ was taken for such a cell because less carbon is needed for the same mass of spinel-$LiMn_2O_4$. The voltage behavior during the first three cycles between 3.0 and 4.0 V of an optimized cell is depicted in Fig. 6. The results obtained from cycling measurements show that this Li-ion cell has an efficiency close to 100% during the 2nd-charge/3rd-discharge cycle. This Li-ion cell exhibits a low initial capacity loss and has successfully passed 50 charge/discharge cycles at the time of writing this paper. It can be remarked that the ohmic resistance of the Li-ion cell decreases upon the repeated cycling. Results obtained on Li-ion cell are in agreement with those reported by Guyomard and Tarascon [29]. They showed that graphite-based cells exhibit a slightly larger capacity and a larger output voltage than coke-based cells.

3.5. *Lithium Diffusion Measurements*

The kinetics of the intercalation/de-intercalation reactions (Eq. 1) of lithium ions in $LiMn_2O_4$ spinel, i.e., chemical diffusion coefficient and thermodynamic factor, have been measured at room temperature by the Galvanostatic Intermittent Titration Technique (GITT) using a Mac-Pile system. The GITT method involves the application of a small current pulse across a Li//$LiMn_2O_4$ cell, while monitoring the transient voltage as a function of time. When the voltage variation was less than 1 mV per hour, the value was defined as the equilibrium potential [30,31].

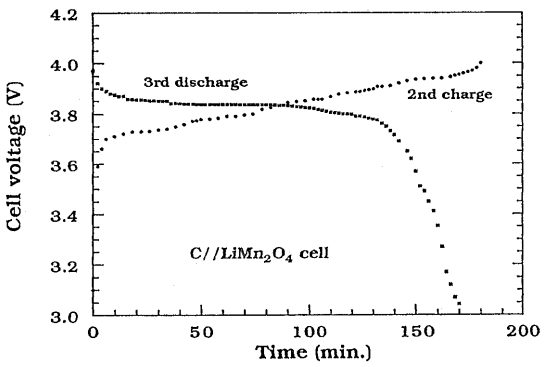

Fig. 6. Galvanostatic multiple charge/discharge curves of a $LiMn_2O_4$//graphite nonaqueous Li-ion rechargeable cell cycled at current densities 0.3 mA/cm^2 (charge) and 0.15 mA/cm^2 (discharge).

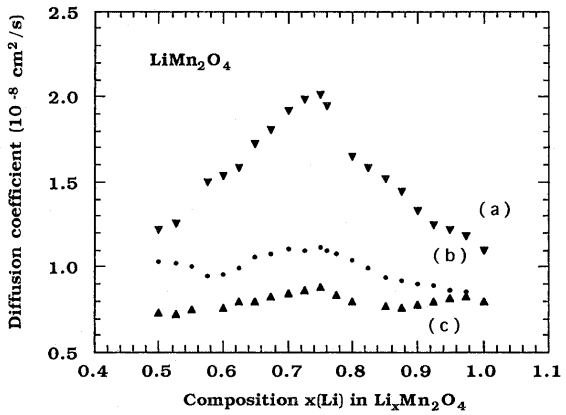

Fig. 7. Chemical diffusion coefficients of lithium ions in $Li_xMn_2O_4$ cathode material as a function of the lithium-ion concentration. (a) first discharge, (b) second charge, and (c) second discharge.

Figure 7 shows the variation of the chemical diffusion coefficient of lithium ions, D_{Li}, as a function of the nominal composition, x(Li). For the first charge-discharge cycle, the values of D_{Li} vary from 2.5×10^{-8} to 1.1×10^{-8} cm^2/s in the compositional range $0.5 \leq x \leq 1.0$, whereas the values of D_{Li} vary from 1.1×10^{-8} to 7×10^{-9} cm^2/s during the second charge. These features reflect the relatively facile insertion process for lithium intercalation in the $LiMn_2O_4$ spinel structure. Moreover, two regions can be discernable in the diffusion-composition curves corresponding to the same trend observable in the titration curve. The curve D_{Li} versus x exhibits a maximum near the value $x = 0.75$. This behavior is indicative of the sequential occupancy of the lithium sites corresponding to the single-phase and the two-phase regions in the charge-discharge profiles. The cubic spinel $LiMn_2O_4$ possesses the Fd3m symmetry, where the Mn cations occupy half of the octahedral sites normally designated 16d and the lithium ions one eight of the tetrahedral 8a sites. Thus, the 16c octahedral empty sites share faces with 8a tetrahedral sites to provide a continuously interconnected interstitial space. It is believed that the Li motion occurs through this type of channel.

By the way, chemical diffusion coefficients of Li ions in the $LiMn_2O_4$ electrode measured using the GITT method also exhibit similar values, of the order of 10^{-8}cm^2/s [32–34]. However, the chemical diffusion coefficients in samples calcined at low temperature are obviously higher than those in samples annealed at high temperature. For instance, $D_{Li} = 4.9 \times 10^{-9}$cm^2/s in samples calcined at 450°C, while D_{Li} is 6.0×10^{-10}cm^2/s in a sample calcined at 1100°C [35]. This difference may be attributed to change in microstructure, domain size, or residual strain of the $LiMn_2O_4$ powder. It seems that our $LiMn_2O_4$ product annealed at 600°C with a quite small domain size of about micrometer possesses higher lithium diffusivity and smaller polarization, indicating the low lattice strain.

4. Conclusion

$LiMn_2O_4$ spinel oxide was synthesized by combustion method with urea as a fuel. This material was successfully tested as lithium battery electrode for cycleability in C//$LiMn_2O_4$ cell using a mixed nonaqueous organic electrolyte. The product $LiMn_2O_4$ was identified as a micron-sized powder. X-ray diagram, Raman and FTIR spectra show that the local environment of the $LiMn_2O_4$ spinel product is in good accordance with the classical structural model of Fd3m space group. Kinetics of intercalation/de-intercalation of Li ions in $Li_xMn_2O_4$ $(0.5 \leq x \leq 1.0)$ were studied using the GITT method. Results show that the chemical diffusion coefficient is in the range $10^{-8} - 10^{-9}$cm^2/s with a weak dependence upon lithium concentration in the host lattice.

Acknowledgments

The authors would like to thank Dr. Saul Ziolkiewicz for fruitful discussions and Mr. Michel Lemal for XRD measurements. This work was partially supported by the Indo-French Center for the Promotion of Advanced Research (IFCPAR) under grant No. 1408-2.

References

1. J.C. Hunter, *J. Solid State Chem.*, **39**, 142 (1981).
2. M.M. Thackeray, W.I.F. David, P.G. Bruce, and J.B. Goodenough, *Mater. Res. Bull*, **18**, 461 (1983).
3. M.M. Thackeray, P. Johnson, L. de Piciotto, P.G. Bruce, and J.B. Goodenough, *Mater. Res. Bull*, **19**, 179 (1984).
4. T. Ohzuku, M. Kitagawa, and T. Hirai, *J. Electrochem. Soc.*, **137**, 769 (1990).
5. D. Guyomard and J.M. Tarascon, *J. Electrochem. Soc.*, **139**, 937 (1992).

6. S.R.S. Prabaharan, M.S. Michael, T. Premkumar, A. Mani, K. Athinarayanaswamy, and R. Gangadharan, *J. Mater. Chem.*, **5**, 1035 (1995).
7. C. Julien, A. Rougier, and G.A. Nazri, *Mat. Res. Soc. Symp. Proc.*, **453**, 647 (1997).
8. I.J. Davidson, R.S. McMillan, J.J. Murray, and J.E. Greedan, *J. Power Sources*, **54**, 232 (1995).
9. F. LeCras, D. Bloch, M. Anne, and P. Strobel, *Mat. Res. Soc. Symp. Proc.*, **369**, 39 (1995).
10. K. Brandt, *J. Power Sources*, **54**, 151 (1995).
11. T. Premkumar, M.S. Michael, P.V.S.S. Prabhu, R. Gangadharan, and S.K. Rangarajan, Indian Patent No.072/Del/93 (1993).
12. V. Manev, A. Kozawa, and N. Momchilova, *J. Power Sources*, **43–44**, 551 (1993).
13. F. Capitaine, P. Graveau, and C. Delmas, *Solid State Ionics*, **89**, 1197 (1996).
14. D. Rahner, S. Machill, H. Schlorb, K. Siury, M. Klob, and W. Plieth, *Solid State Ionics*, **86–88**, 891 (1996).
15. J.M. Tarascon, E. Wang, F.K. Shokoohi, W.R. McKinnon, and S. Colson, *J. Electrochem. Soc.*, **138**, 2559 (1991).
16. S.R.S. Prabaharan, M.S. Michael, and R. Gangadharan, Indian Patent No. NF-244/95 (1995).
17. S.S. Manoharan and K.C. Patil, *J. Am. Ceram. Soc.*, **75**, 1012 (1992).
18. S. Chitra, P. Kalyani, T. Mohan, R. Gangadharan, and C. Julien, Indian Patent (1999) under process.
19. D. Briggs and M.P. Seah, *Practical Surface Analysis by Auger and XPS*, (Wiley, New York, 1985), p. 37.
20. Joint Commission on Powder Diffraction Standards (JCPDS) card No. 35–782, International Center for Diffraction Data, Newtown Square, PA 19073.
21. M.M. Thackeray, P. Johnson, L. de Piciotto, P.G. Bruce, and J.B. Goodenough, *Mater. Res. Bull.*, **19**, 179 (1984).
22. D. Guyomard and J.M. Tarascon, *J. Electrochem. Soc.*, **138**, 2864 (1991).
23. G.C. Allen and M. Paul, *Appl. Spectrosc.*, **49**, 451 (1995).
24. C. Julien, C. Perez-Vicente, and G.A. Nazri, *Ionics*, **2**, 1 (1996).
25. G. Pistoia, D. Zane, and Y. Zhang, *J. Electrochem. Soc.*, **142**, 2551 (1995).
26. C. Julien, M. Massot, C. Perez-Vicente, E. Haro-Poniatowski, G.A. Nazri, and A. Rougier, *Mat. Res. Soc. Symp. Proc.*, **496**, (1998).
27. J. Preudhomme and P. Tarte, *Spectrochim. Acta*, **27A**, 845 (1971).
28. G.J. Exarhos and W.N. Risen, *Solid State Commun.*, **11**, 755 (1972).
29. D. Guyomard and J.M. Tarascon, *Solid State Ionics*, **69**, 222 (1994).
30. W. Weppner and R.A. Huggins, *J. Electrochem. Soc.*, **124**, 1569 (1977).
31. C. Julien, in M. Balkanski (Ed.), *Microionics-Solid State Integrable Batteries* (North-Holland, Amsterdam, 1991), chap. 3.5, p. 307.
32. L.Q. Chen, X.J. Huang, E. Kelder, and J. Schoonman, *Solid State Ionics*, **76**, 91 (1995).
33. M.Y. Saidi, J. Barker, and R. Koksbang, *J. Solid State Chem.*, **122**, 195 (1996).
34. M. Wakihara, G.H. Li, H. Ikuta, and T. Uchida, *Solid State Ionics*, **86–88**, 907 (1996).
35. L. Chen and J. Schoonman, *Solid State Ionics*, **67**, 17 (1993).